DIVERTOR CONFIGURATION AND HEAT LOAD STUDIES FOR THE ARIES-CS FUSION POWER PLANT

T. K. MAU,*[a] T. B. KAISER,[b] A. A. GROSSMAN,[a] A. R. RAFFRAY,[a] X. R. WANG,[a]
J. F. LYON,[c] R. MAINGI,[c] L. P. KU,[d] M. C. ZARNSTORFF,[d] and ARIES-CS TEAM

[a]*University of California, San Diego, La Jolla, California 92093*
[b]*Lawrence Livermore National Laboratory, Livermore, California 94551*
[c]*Oak Ridge National Laboratory, Oak Ridge, Tennessee 37831*
[d]*Princeton Plasma Physics Laboratory, Princeton, New Jersey 08543*

Received May 1, 2007
Accepted for Publication October 5, 2007

The critical issue of divertor configuration for heat and particle flux control in a conceptual ARIES compact stellarator (CS) reactor is addressed. The goal is to determine a divertor location and geometry with a peak heat load of not more than 10 MW/m^2 for a CS equilibrium based on the configuration to be used in the NCSX experiment, optimized for high beta (6.4%) and designed for low alpha-particle power loss fraction (≤5%). The surface heat flux on the target has three components: thermal particles, lost energetic alphas, and radiation from the core and the scrape-off layer. The first two components are dominant and their magnitudes can be comparable. To maintain a tritium-breeding ratio of 1.1, the total target area should not exceed 15% of the boundary plasma surface area. The divertor concept consists of two pairs of target plates per field period, one pair each at the top and bottom of the plasma. The heat flux profile is assessed by assuming that the parallel transport can be represented by field line mapping and that cross-field transport can be modeled with a prescribed field line diffusion scheme. In this manner, the poloidal and toroidal extents of the plates and their shape and distance to the plasma are designed to intercept all the heat flux and to minimize the peak thermal heat load. An approximate scheme, based on particle drift orbits in the core and field line tracing in the edge, is derived to estimate the alpha-particle heat load distribution over the plates and the first wall. The best plate configuration to date yields total peak heat loads (thermal + alpha) ranging from 5 to 18 MW/m^2. Further optimization of the target plates is required to reach the design goal, which will be addressed in a future study.

KEYWORDS: *divertor, heat load, fusion power plant*

Note: The figures in this paper are in color only in the electronic version.

I. INTRODUCTION

The ARIES compact stellarator (ARIES-CS) Advanced System Studies[1] is a multiyear, multi-institution project aimed at assessing the potential of the compact stellarator magnetic confinement concept as an attractive fusion power plant. Research is initially focused on identifying an optimum plasma configuration that meets the physics performance goals and engineering constraints, leading to a safe and economically viable reactor. Desirable features that determine the overall reactor size and cost include high plasma beta, well-confined particle orbits, low aspect ratio, comparatively simple coil set, and sufficiently small plasma-coil distance. An integrated design of a power plant based on this configuration is carried out, for which an optimum plasma operating point is determined. To consolidate the design effort, the issue of particle and heat flux control beyond the last well-defined magnetic flux surface must be addressed. The present paper investigates the use of divertors to solve this critical problem for the ARIES-CS fusion power plant.

*E-mail: mau@alisa.ucsd.edu

The divertor configuration is highly dependent on the magnetic field structure at the plasma boundary, and its operation is closely linked to the confinement performance of the core plasma. For a stellarator, this boundary is complicated and three-dimensional (3-D) in space, implying that a highly effective target configuration must have a conformal 3-D geometry. Three major divertor concepts have been investigated in experiments[2] and with physics modeling codes.[3] In moderate- to high-shear heliotrons, such as CHS (Ref. 4) and LHD (Ref. 5), intrinsic helical diverting field lines are used to create a helical divertor. Also in these devices, additional field perturbation coils are installed to create imposed edge magnetic islands that are intersected by target plates to form so-called local island divertors (LIDs). In recent experiments on LHD (Ref. 5), the basic functions of the LID concept, such as edge plasma control with effective pumping and impurity control, were demonstrated. Divertors of the third type based on intrinsic island structures are found in low-shear Helias devices such as W7-AS (Ref. 6) and W7-X (Ref. 7). The best results to date were obtained in W7-AS (Ref. 6) with 10 open island divertor modules. In this experiment, a neutral beam–heated, high-density ($n_e \sim 3.5 \times 10^{14}$ cm^{-3}) operating regime, with energy confinement times increasing steeply with density and particle and impurity confinement times decreasing with density, was reported. This resulted in full density control and quasi-steady-state operation under the condition of partial detachment from the divertor targets, accompanied by up to ~90% radiation fraction at the plasma edge. Peak heat loads of 3 (8) MW/m^2 were measured with a 5- (3-) cm full-width at half-maximum value on selected targets[8] and were related to the incident angle of the flux to the plate surface.

Divertor modeling for stellarators was first explored with the technique of field line tracing from the plasma boundary to the target plates,[9] and the resultant density of strike points gives an estimate of the heat load distribution. Solution of the parallel transport equation in the edge region[10] is then used to relate the target and upstream plasma parameters. A more detailed modeling approach involves numerically solving a set of fluid transport equations in the 3-D edge magnetic geometry. In the EMC3 code[11] the Monte Carlo technique is used that requires the appropriate choice of coordinates to clearly identify the field line parallel direction and extends the analysis to cover stochastic field structures. In its latest version, the finite flux tube coordinates are employed and the reverse field line–mapping technique is applied to facilitate coordinate transfer between regions of different computational meshes. This code, coupled with the EIRENE neutral transport code, has successfully predicted a number of physics results of the W7-AS island divertor experiment[6] and of the LID experiment on LHD (Ref. 5).

Divertor research to date for the National Compact Stellarator Experiment[12] (NCSX), a quasi-axisymmetric device under construction, has been centered on magnetic topology study at the plasma boundary.[13] The edge magnetic field was mapped via field line tracing in a finite-beta equilibrium in which ~20% of the flux is due to the plasma bootstrap current. Proceeding outward from the last closed magnetic surface, the field lines make a transition from ergodically covering a volume to becoming moderately stochastic, with significant flux expansion at the top and bottom of the bean-shaped cross section and weak signatures of $m/n = 5/3$ island structures.[14] Based on these studies, initial target plate locations have been identified.[15]

In this paper, a divertor configuration is determined for the ARIES-CS integrated fusion power plant conceptual study that satisfies a number of physics and engineering criteria. The present work, which uses the field line–tracing technique, is the continuation of an earlier exploratory study.[16] The reference plasma configuration is extrapolated from the NCSX base equilibrium with reactor-relevant modifications. The heat load distribution on the set of target plates is calculated by including contributions from both the thermal fuel plasma and the escaping energetic alpha particles. Section II highlights the physics and engineering design criteria for the divertor system, some of which are pertinent to the reference reactor design point. The main analysis tool used in the design, a field line–tracing code, is also described. In Sec. III, the process of determining the divertor plate location and surface geometry using the design codes is discussed, from an initial flat plate to a simple curved shape, with corresponding heat load distribution on the plates. Section IV describes the reference target plate geometry after some optimization based on minimizing the thermal peak heat load. This is followed by a presentation of an approximate model for the alpha-particle heat flux and the corresponding alpha heat load distribution on the targets in Sec. V. Section VI then gives an account of the total heat load distributions by combining the results from thermal and alpha fluxes. In Sec. VII, the results are summarized, followed by a list of suggestions for improving on the present calculations.

II. DIVERTOR DESIGN CRITERIA AND ANALYSIS TOOL

This study addresses the question: Given an optimized CS plasma equilibrium,[17] can there be a divertor target plate configuration with a heat load distribution that satisfies a reasonable set of engineering constraints? Specifically, the heat load has two major components: thermal particles and energetic (non-Maxwellian) particles. The thermal component arises from conductive and convective heat losses past the last closed magnetic surface (LCMS) where field lines become stochastic, while the energetic part comes from those slowing-down alpha particles that cross the plasma surface before full equilibration with the background plasma. In a steady-state

device, the heat load on the target plate is constrained by the choice of materials (thermomechanical properties). For the He-cooled W alloy divertor design in this study, the peak heat load should be limited to 10 MW/m^2 (Ref. 18). Since the divertor system disrupts the surrounding blanket and shield near the surface, negatively affecting its tritium breeding capability, two further constraints must be satisfied to achieve an overall breeding ratio of 1.1 (Ref. 19):

1. The targets must cover less than 15% of the first wall area.

2. The targets need to be located sufficiently far from the outboard midplane region, where the neutron flux is the highest.

Conceptually, the divertor consists of an array of target plates around the torus between the plasma and the first wall, at some radial distance from the LCMS to inhibit impurity influx from the scrape-off layer (SOL) region back into the core. The divertor plates are used primarily to intercept thermal particle and heat fluxes escaping from the plasma, to help remove the collected heat by coolant flowing underneath them, and to control the particle density via pumping and appropriate placement of baffle plates. To design a target plate that will meet all of these requirements, it must satisfy the following criterion:

$$P_{div}/A_D < W_{lim}/\eta \ , \tag{1}$$

where P_{div} is the thermal power reaching the plate, A_D is the plate total area, W_{lim} is the design peak heat load limit, and η is the heat load peaking factor. The choice of the surface and structural materials and the coolant together with its flow path determines the value of W_{lim} (Ref. 18). In an optimum divertor configuration, the placement and surface topology of the target plates should result in the lowest possible η, thus allowing the divertor to handle high heat loads with the least amount of high-Z plate material. On the other hand, noting that the thermal divertor power is

$$P_{div} = (1 - f_{rc} - f_{\alpha})(1 - f_{rd})P_{\alpha} \ , \tag{2}$$

where P_{α} is the fusion-produced alpha power, f_{rc} is the core radiation fraction, f_{α} is the alpha power loss fraction, and f_{rd} is the fraction of power radiated from the divertor/SOL region, the divertor power can be reduced by operating with higher core and SOL radiation. The former condition may be achieved by setting up a radiating mantle just inside the LCMS, whereas the latter condition may require the divertor to operate in the high-recycling or partially detached regime with the right combination of density, temperature, and impurity content in front of the plate. Coupled to this criterion is the need to ensure that the connection length L_C between the plasma midplane and the plate is sufficiently long to permit a substantial level of radiation to occur in the divertor region. Using the Borrass two-point model,[20] an operational window has been found for $L_C \approx 100$ to 300 m and $f_{rd} > 60\%$ with $T_{e,div} \approx 15$ to 20 eV, $n_{e,div} \approx 4$ to 6×10^{14} cm^{-3}, $T_{e,sep} \approx 200$ to 300 eV, $n_{e,sep} \approx 6$ to 8×10^{13} cm^{-3}, and using a 2.5 to 5.0% carbon impurity concentration to mimic radiation levels for other materials such as neon. These conditions are similar to those expected in reactor-scale plasmas.

Because of the complex 3-D magnetic geometry inherent in a stellarator, a suite of large analysis codes is used to carry out the divertor studies as indicated in Fig. 1. The combination of VMEC (Ref. 21) and MFBE (Ref. 22) calculates the magnetic field on a 3-D grid both inside and outside the LCMS, including finite plasma β effects such as the bootstrap current. The field

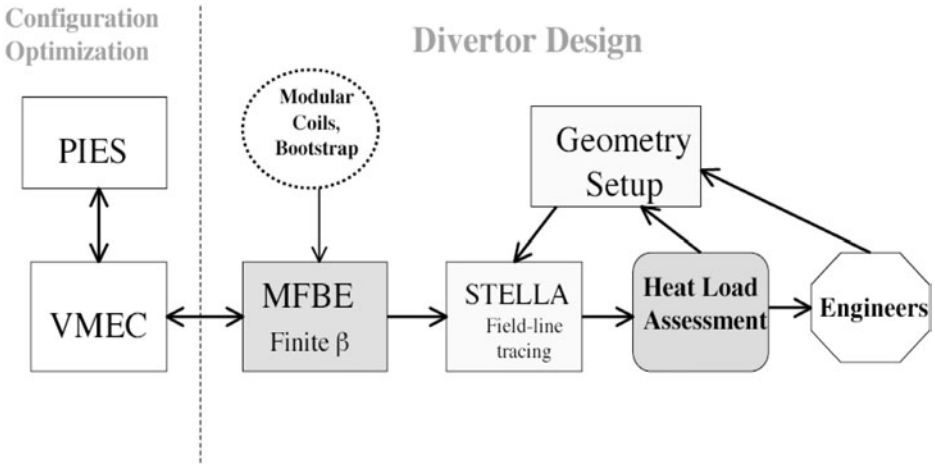

Fig. 1. Divertor design tools and strategy used for ARIES-CS analysis.

line tracing code, STELLA-FL (Ref. 23), is an interactive computational tool that analyzes magnetic fields and estimates heat loads on divertor structures and vacuum vessel walls in stellarators. As input STELLA-FL accepts magnetic field data on an (R, Z, ϕ) grid in either PIES or VMEC/MFBE format, vacuum vessel data in Fourier component (VMEC) form, and divertor data as the coordinates of a set of points locating the corners of the quadrilateral segments that compose each target plate.

Magnetic field lines are followed from an arbitrary set of starting points, for example, equally spaced in arc length on a shell conformal with the LCMS until they intersect a divertor structure or the vacuum vessel or exceed a user-prescribed length. Field lines are traced by integrating the field line equations in (R, Z, ϕ) coordinates with respect to distance s along the line,

$$\frac{dR}{ds} = \frac{B_R}{B} \quad , \quad \frac{dZ}{ds} = \frac{B_Z}{B} \quad , \quad \frac{d\phi}{ds} = \frac{1}{R}\frac{B_\phi}{B} \quad , \qquad (3)$$

using either a fourth-order Runge-Kutta or an Adams-Bashforth predictor-corrector scheme, with relative (cumulative) errors constrained to be less than a user-specified threshold, typically 10^{-5}. The direction of integration can be either parallel or antiparallel to the magnetic field. The effect of particle scattering and cross-field transport is simulated by perpendicular diffusion of field lines, with a specified diffusion coefficient $D_\perp$. Interpolation of the vector magnetic field is done using arbitrary-order (typically fifth) B splines. Intersection of field lines with either divertor plate segments or the first wall is determined by monitoring a function that vanishes only on the structures of interest.

Heat loads on divertor plates or the wall are estimated by assuming that each field line carries an identical increment of power, $P = P_{loss}/N$, where N is the total number of field lines traced and P_{loss} is the particle power loss from the plasma assuming no power source or sink along the entire line length. For simplicity, consider an ideal one-plate divertor system that intersects all the field lines. The target area A_D is divided into $n_\theta \times n_\phi$ segments. The heat load W_j to each plate segment j of area A_j located at (θ, ϕ) due to N_j number of field lines striking the region is then

$$W_j(\theta, \phi) = \left(\frac{N_j}{N}\right) P_{div}/A_j \quad . \qquad (4)$$

Here, the effect of the angle of incidence (α) of the field line to the segment surface is implicitly included in the number of field lines intercepted $(N_j \sim \sin\alpha)$. The peaking factor η_j for each segment is defined as

$$\eta_j(\theta, \phi) = W_j/(P_{div}/A_D) = (N_j/A_j)/(N/A_D) \quad , \qquad (5)$$

and the heat load peaking factor for the entire plate is given by $\eta = \max\{\eta_j\}$ for $1 \le j \le n_\theta \times n_\phi$. The peak heat load on the plate is then $W_{pk} = \eta P_{div}/A_D$. It follows that to minimize W_{pk}, it is necessary to lower η and P_{div} and increase A_D. These definitions can easily be extended to a nonideal set of target plates, as is the case in this study, keeping in mind that the power absorbed by each plate is proportional to the number of field lines it intersects.

In STELLA-FL (Ref. 23), several diagnostics are computed for each field line, including connection length, angle of incidence, and strike point location. A number of graphical diagnostics are also generated, including strike point locations on divertors and the wall, contour and 3-D perspective plots of heat load and peaking factor, connection length and angle of incidence distributions, and a variety of Poincaré plots of puncture points that field lines make with toroidal planes.

III. DIVERTOR PLATE LOCATION AND SURFACE TOPOLOGY

The general strategy for divertor design is as previously shown in Fig. 1. First, the divertor is to be defined on a plasma configuration that is optimized for high beta and low alpha-particle loss fraction. The magnetic geometry is therefore not specifically tailored for the island divertor concept that requires the setting up of distinct island structures outside the last closed magnetic surface, as was found in LHD (Ref. 5) and W7-AS (Ref. 6). Second, the initial location, size, and orientation of the target plates are determined based on field line–tracing considerations to maximize interception of field lines and to minimize the peak heat load. Third, the target plate geometry is adjusted or optimized to accommodate the thermal loss power while satisfying the peak heat load limit.

For the ARIES-CS divertor study, an NCSX-based magnetic configuration[12] created in the first phase of the project is used that has three toroidal field periods, 18 modular coils, $\beta = 4\%$, and an aspect ratio $A = 4.5$. The scaled-up reactor has $\langle R \rangle = 8.25$ m, $\langle a \rangle = 1.85$ m, $B = 5.3$ T on-axis, and a net electric power output of 1 GW(electric). In comparison, the final reference equilibrium configuration[17] has $\langle R \rangle = 7.75$ m, on-axis $B = 5.7$ T, $\beta = 6.4\%$, and $A = 4.5$. Dimensionless quantities such as the peaking factor should be preserved, since the basic features of the edge magnetic topology between the two configurations are sufficiently similar. To evaluate heat loads, the size of the divertor plates is scaled with the plasma surface area to the reference configuration, as indicated later in this paper. At the reference plasma operating point,[24] it is assumed that the core and divertor radiation fractions $f_{rc} = f_{rd} = 75\%$ and the alpha power loss fraction $f_\alpha = 5\%$. Power balance leads to 23.6 MW of thermal particle power and 23.6 MW of alpha-particle power reaching the divertor. As will be shown, a large fraction of this power will strike the target plates, with the rest reaching the plate shadow region (between the

plate backside and the wall) or directly hitting the wall. A small amount of radiation power will also strike the target plates in a uniform fashion, which is not considered in this paper.

To provide initial guidance for target placement, a Poincaré plot of field lines outside the LCMS at the $\phi =$ 0 deg toroidal plane, shown in Fig. 2, is first examined. The traced field lines are ergodic, mapping out a volume of finite radial width. The region outside the tips of the bean-shaped cross section is desirable for locating the target plate for two reasons. First, as indicated in Fig. 2, there are many more field line crossings here than in the rest of the circumference, increasing the probability of field line interception by obstacles in this region. Second, significant flux expansion is observed in the same region that facilitates surface spreading of the heat load. Also, to keep the intersection angles small for spreading the heat load, the plates are initially placed on an imaginary surface approximately conformal to the LCMS. Shown in Fig. 2 are two pairs of plates, one pair each at the top and at the bottom. Strictly speaking, this configuration does not constitute a divertor but a limiter because no *X*-point is created. However, in the high–flux expansion cross section, the plasma behaves as if a magnetic null has been imposed, leading one to refer to it as a divertor. It is also important to note that away from the divertor region, the first wall has to be sufficiently distant from the plasma surface to prevent it from intercepting the field lines before they diffuse past the divertor radial location.

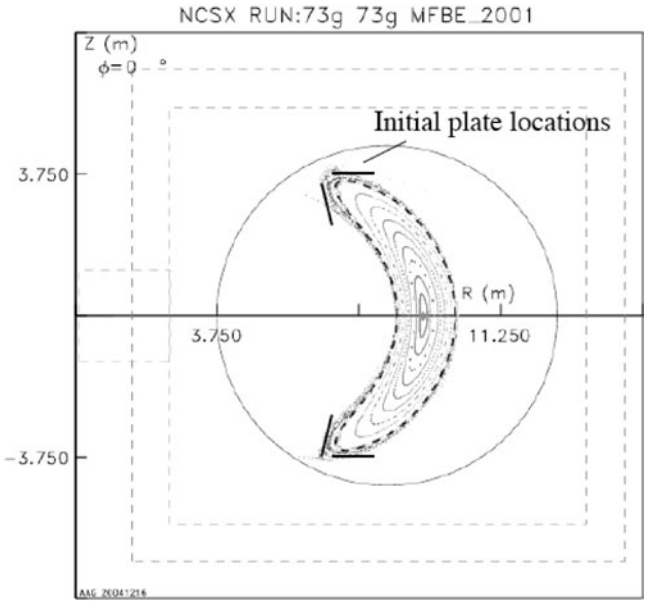

Fig. 2. Poincaré plot of field line puncture points (blue/green dots) on $\phi = 0$ deg minor cross section and probable location of divertor plates (thick black solid lines). Also shown are closed flux surfaces (red lines) and LCMS (black dashed line). (Color online)

For modeling the thermal heat flux, field lines are launched from a surface conformal to and at a short radial offset distance inside the LCMS at $\phi = 0$, 30, 60, and 120 deg. Here stellarator symmetry is invoked that allows one to launch field lines only from one field period, 0 deg $\leq \phi \leq$ 120 deg, and translate all final strike points on the plasma facing components (PFCs) to that period. In the present study, the starting points are uniformly spaced along the surface. For each field line launched in one direction, there is a corresponding one launched in exactly the opposite direction. Cross-field diffusion of the heat flux is modeled by a radial diffusivity set to $D_\perp = 1.0$ m^2/s, which is well within the range observed in many experiments. In essence, for every incremental advance, Δs, in field line length, there is a random transverse displacement given by $\delta R = \delta\rho \cos(2\pi\eta')$, $\delta Z = \delta\rho \sin(2\pi\eta')$, with $\delta\rho = (12 D_\perp \Delta s/v_{th})^{1/2}\zeta$ and ζ, η' being uniformly distributed in $[0,1]$. The factor 12 in the expression for $\delta\rho$ is chosen to insure that the field line spreading is consistent with isotropic two-dimensional perpendicular diffusion governed by $D_\perp$.

The first set of plates tested have a flat profile when projected on the minor cross section, with their end points located on a conformal surface 15-cm offset from the LCMS, as illustrated in Fig. 3. These plates all have a poloidal extent of $\Delta\theta = 20$ deg, are centered at $\phi = 0$ deg, and extend from $\phi = -25$ deg and $\phi = +25$ deg. The toroidal extent of the plates is limited by the blanket/shield/coil radial build at locations beyond $\phi = \pm 25$ deg. A test run with 16 000 field lines results in 93.5% intersecting the plates, 6.2% entering the shadow region, and 0.3% striking the wall. The strike point patterns on the plate surfaces are shown in Fig. 4, where ξ and ζ are the normalized coordinates in the toroidal and poloidal directions, respectively, for each plate. The footprints on each plate are roughly divided into two physically separate groups, each corresponding to field lines traced in one toroidal direction. The average field line length from start to plate interception is calculated to be 233 m, which is four to five times the plasma toroidal circumference, and the average angle of field line inclination to the surface is 5.5 deg with a range of 0 to 11 deg.

Since the STELLA-FL code assumes stellarator symmetry, the plate geometry also exhibits the same symmetry as expected. For the purpose of displaying results, each plate is divided into two toroidal half-plates, one encompassing the toroidal extent of -25 deg $\leq \phi <$ 0 deg, denoted $(-)$, and the other covering $0 \leq \phi \leq$ $+25$ deg, denoted $(+)$. Using the notations L, U, O, and I to represent lower, upper, outboard, and inboard, respectively, an upper, outboard half-plate spanning 0 deg $\leq \phi \leq +25$ deg is denoted as UO$(+)$, etc. Subdividing each half-plate into 30×60 grid points, the calculated peaking factor profile for the LO$(+)$ half-plate is displayed, as an example, in Fig. 5, where the peaking factor for the entire half-plate is 10.9. The

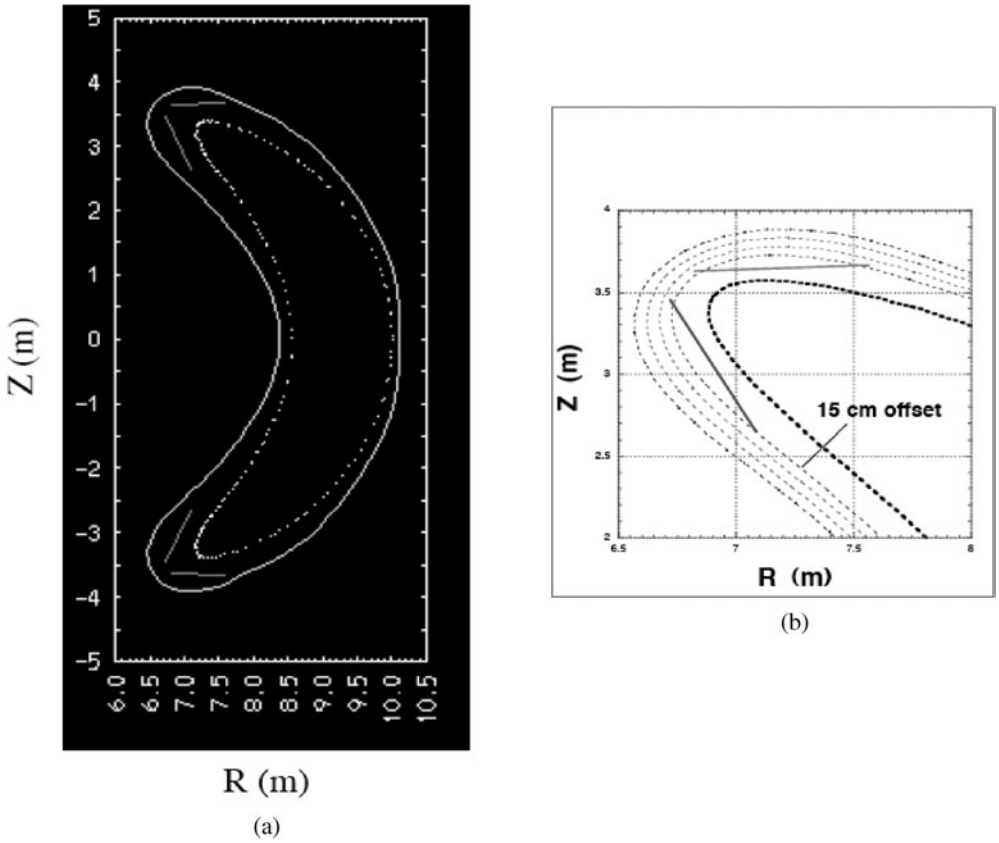

Fig. 3. (a) Flat divertor plates (red), first wall (green), and field line start points (white) projected on $\phi = 0$ deg minor cross section. (b) Close-up of upper divertor plates; black dotted line shows the LCMS based on VMEC, and the other dotted lines show offset conformal surfaces at 5-cm interval, starting from a 15-cm offset distance. (Color online)

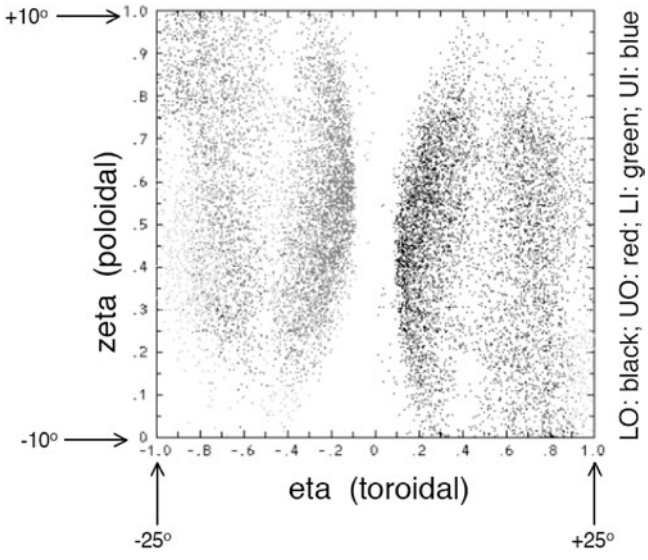

Fig. 4. Field line strike points on the four target plates plotted in (ξ, ζ) normalized space for each plate. (Color online)

thermal heat load distributions for the eight half-plates in each field period are given in Table I, where the half-plate surface areas have been scaled to correspond to a major radius of 7.75 m at the same aspect ratio of 4.5. It is observed from this table that the outboard (OB) plates intercept about three-quarters of the thermal power that hits the target plates, resulting in a peak thermal heat load of 13.8 MW/m^2 on these plates. On the other hand, the peak heat load on the inboard (IB) plates is calculated to be 3.8 MW/m^2.

Next, the idea of lowering the peak heat load on the OB plates by rectifying the imbalance of heat flux interception between IB and OB plates is investigated. This is achieved by moving the end points of the OB plates radially outward to 20-cm offset from the LCMS and those of the IB plates inward to 10-cm offset. This plate arrangement results in a 46 : 54% distribution of heat between the OB and IB plates, with respective peak heat loads of 11.5 and 11.0 MW/m^2. This indicates that moving the OB plates farther away from the plasma allows more field lines to have access to strike

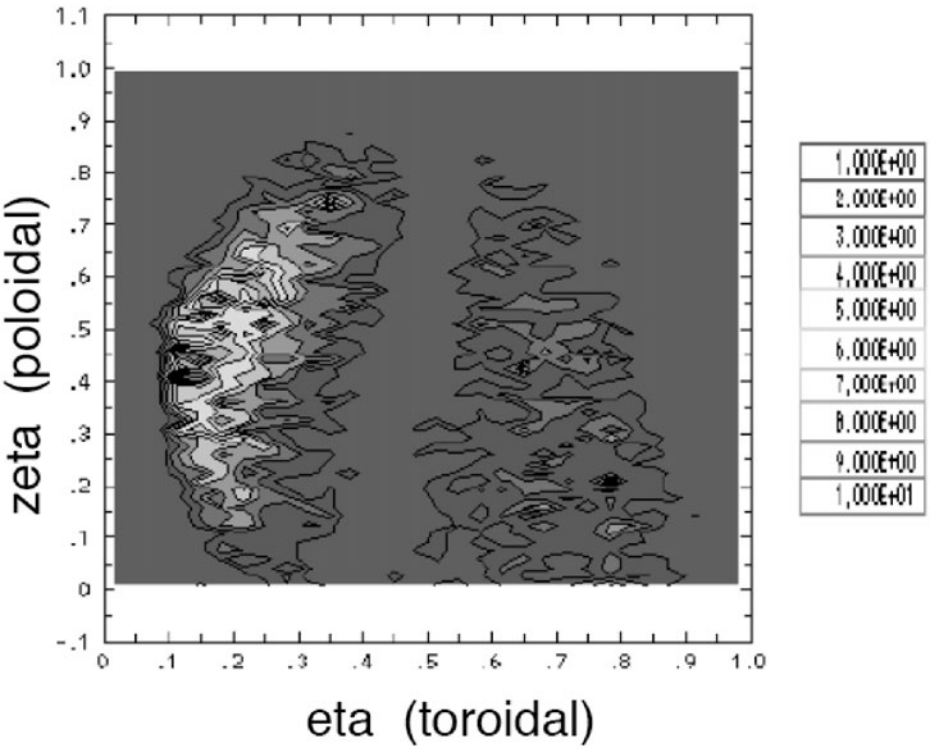

Fig. 5. Peaking factor profile in (ξ, ζ) space for LO(+) half-plate.

TABLE I

Thermal Heat Load Distribution for Flat Plate Case

Target Half-Plate	Area[a] (m^2)	Load Fraction	Peaking Factor	Incident Power (MW)	Peak Heat Load (MW/m^2)
Lower OB (+)[b]	2.08	0.354	10.9	2.64	13.8
Lower OB (−)[c]	1.62	0.016	42.3	0.12	3.1
Upper OB (+)	1.62	0.016	42.3	0.12	3.1
Upper OB (−)	2.08	0.352	10.9	2.62	13.7
Lower IB (+)	2.36	0.021	37.6	0.15	2.4
Lower IB (−)	2.11	0.110	10.0	0.82	3.8
Upper IB (+)	2.11	0.110	10.0	0.82	3.8
Upper IB (−)	2.36	0.021	37.6	0.15	2.4

[a]Sealed to $\langle R \rangle = 7.75$ m.
[b](+) = 0 deg $\leq \phi \leq$ 25 deg.
[c](−) = −25 deg $\leq \phi <$ 0 deg.

the IB plates after a number of revolutions around the torus.

It is noted that for flat plates, adjusting the radial locations of the plates for equal heat load distribution is insufficient for reducing the peak thermal load below the prescribed limit. Thus, additional tailoring of the surface topology may be necessary to smooth out local peak loads, which is equivalent to making the target surface more conformal to the LCMS. This is accomplished by moving the midpoint of the previously used flat plate radially outward on the poloidal plane while keeping the end-point locations fixed. Specifically, the midpoints of the OB and IB plates are fixed at 12 and 5 cm from the plasma surface, respectively, in this case study. This

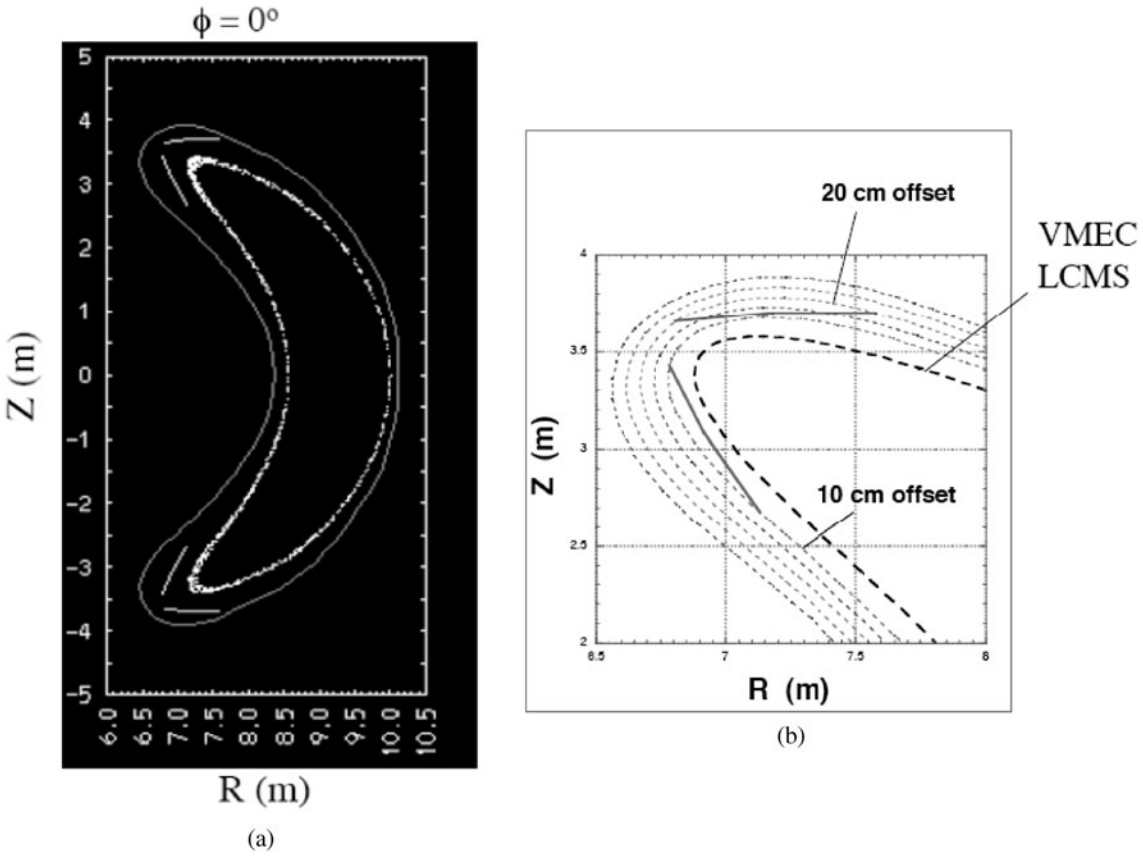

Fig. 6. (a) Reference plates (green), wall (red), and Poincaré plot of field lines outside LCMS projected on $\phi = 0$ deg plane. (b) Close-up of upper plates; dashed colored lines are conformal surfaces with VMEC LCMS. (Color online)

results in the heat flux being equally distributed between the IB and OB plates, and the peak heat loads are reduced to 10.7 and 7.8 MW/m^2 on the OB and IB plates, respectively. Thus, adjustments in the locations and surface topologies of the plates can improve the target plate power distribution to achieve a desired peak heat load.

IV. REFERENCE DIVERTOR CONFIGURATION AND THERMAL HEAT LOAD DISTRIBUTION

For the ARIES-CS power plant, divertor studies are focused on a reference plate configuration that results from several iterations of plate for the best heat load performance to date. The projection of the plates onto the minor cross section at $\phi = 0$ deg is shown in Fig. 6, where the plate surface profile is represented by three points. An isometric view of the plate geometry for one field period is shown in Fig. 7, where the eight half-plates are labeled. For this configuration, the typical poloidal width and toroidal length of a plate are 0.8 and 2.9 m, respectively. The surface area of the plates for the entire

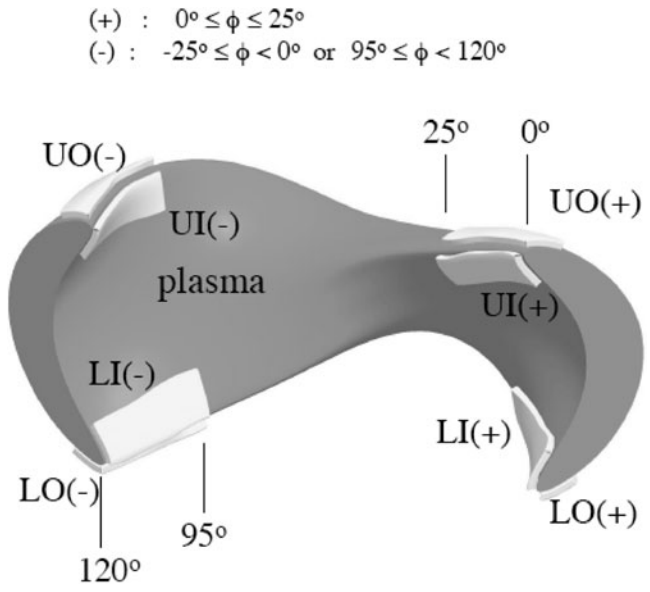

Fig. 7. Isometric view of reference divertor plates in one field period.

torus, scaled to $R = 7.75$ m, is 50 m^2, which is equal to 7% of the plasma surface area. For the analysis, each half-plate is subdivided into 60×60 segments. Two such segments will constitute an individual helium-cooled T-tube divertor unit[25] that has dimensions of 1.5 cm $\times$ 10.0 cm.

Before proceeding to a detailed assessment of the thermal heat load on the plates, the number of launched field lines sufficient to give an accurate statistical representation of the heat deposition profiles is first determined. As a measure of this accuracy, the standard deviation representative of a Gaussian distribution/normal distribution, i.e., $\sigma = M^{-1/2}$, is invoked, M being the number of strike points on the segment where the peak heat load is located. An extensive analysis of the effect of the number of launched field lines, N, on the peak heat loads on the various plates is carried out. The traced field lines will end up on the plates, in the shadow region, or on the first wall. Depending on how far the plates are located radially from the start points, a fraction of the field lines will exceed a certain prescribed length, typically 2000 m, and tracing will be terminated. For these field lines, it is assumed that the power carried is radiated entirely before striking any target and is not considered part of the incident power. The field lines that strike any object are relatively unevenly distributed among the plates. For those half-plates that intercept the most field lines, the peaking factors (and peak heat loads) converge toward lower values rather quickly as N is increased and as $M^{-1/2}$ decreases, whereas for those with a lesser number of strike points, the convergence is much slower. The distribution of strike points among plates, shadow region, and wall is relatively constant as N is varied. There is also a practical limit to the number of field lines that can be traced, which is determined by the real time it takes to set up the input data, run the code serially, and process the output data into numerical results and graphical displays that can be used.

The reference case is computed to the practical limit, where 128 000 field lines are launched, with 107 631 lines actually hitting the plates (89.6%), shadow region (10.3%), or wall (0.1%), with the remainder exceeding the prescribed maximum field line length. The strike point patterns on the four plates in each field period are shown in Fig. 8. It is apparent that the footprints exhibit stellarator symmetry between the pairs of OB and IB plates as expected, since the launching of field lines and the plate configuration also follow symmetrical patterns. The bright strip along the midpoint of the plates is indicative of that region being farthest away from the plasma and thus geometrically shielded from the field lines. The heat load distribution among the half-plates is given in Table II, which shows no strike points on the UO(+) and LO(−) half-plates. For this reference divertor configuration, the IB and OB plates intercept equal amounts of the thermal heat. The two OB plates have the highest peak heat load, both at 10.4 MW/m^2. These correspond to a peaking factor of about 13 ± 1.4. As an illustration, in Fig. 9, the peaking factor profile $\eta(\theta, \psi)$ for the LO(+) half-plate indicates the location of the peak heat load point.

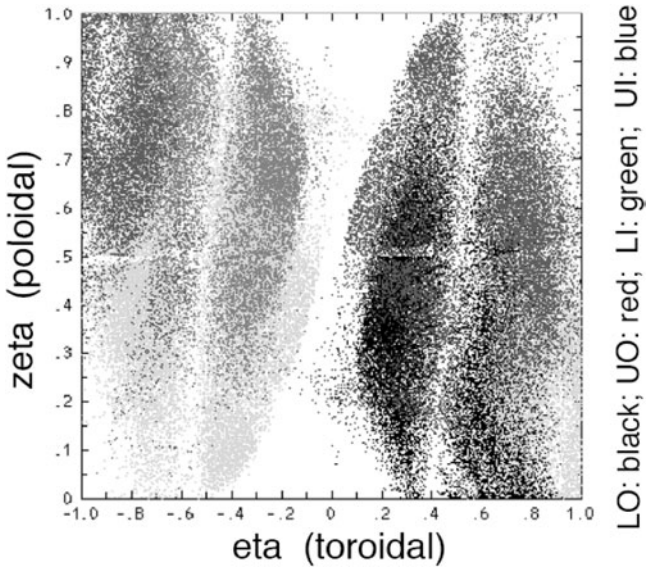

Fig. 8. "Thermal" field line strike points on reference divertor plates plotted in (ξ, ζ) space. (Color online)

V. ASSESSMENT OF DIVERTOR HEAT LOAD DUE TO ENERGETIC ALPHA PARTICLES

Because of the nonaxisymmetry of the CS magnetic topology, a large number of alpha particles either are born on unconfined trajectories that result in prompt losses from the plasma at close to their birth energy of 3.5 MeV or are pitch-angle scattered into ripple-trapped orbits that cause their exit from the plasma before they fully equilibrate with the background plasma. The resultant loss of alpha heating power would lead to a higher confinement H-factor required for the equilibrium operating point. The major impact, however, is in the potential damage to the surfaces of the PFCs where these energetic alpha particles strike. To reduce these particle losses to an acceptable level, the magnetic topology of the plasma equilibrium has been modified to minimize the ripple well depth in the plasma core, and the density (temperature) of the plasma has been raised (lowered) to increase the collisional drag on the slowing alphas.[17] As a result of these optimization steps, an alpha power loss fraction f_α of 5% or less has been achieved. This results in a kinetic power of $f_\alpha P_\alpha$ impinging on the divertors, in addition to the thermal power P_{div} given in Eq. (2).

To critically assess the impact of these lost alphas on the PFCs, it is necessary to determine the fractions of these particles striking the divertor plates and first wall

TABLE II

Thermal Heat Load Distribution on Reference Divertor Plates

	Half-Plate					
	LO(+)	UO(−)	LI(+)	LI(−)	UI(+)	UI(−)
Load fraction (%)	24.7	25.0	6.7	18.3	18.4	6.7
Incident power (MW)	1.74	1.76	0.47	1.29	1.30	0.48
Area (m^2)	2.20	2.20	2.20	2.02	2.02	2.20
Average load (MW/m^2)	0.79	0.80	0.21	0.64	0.64	0.22
Peaking factor (60×60)	13.13	12.99	19.24	9.63	9.60	19.08
Standard deviation	0.11	0.11	0.19	0.16	0.16	0.19
Peak heat load (MW/m^2)	10.38	10.40	4.14	6.15	6.16	4.16

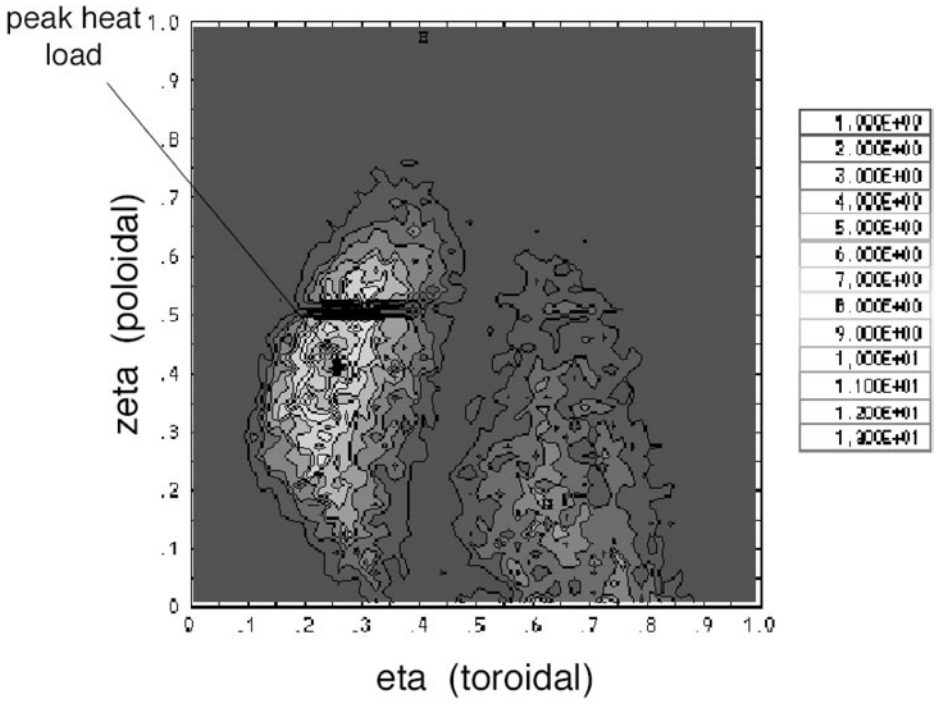

Fig. 9. Peaking factor profile for thermal heat load in LO(+) half-plate in (ξ, ζ) space.

and the resulting heat load distributions on their surfaces. In the absence of a fully integrated set of analysis tools for this purpose, the STELLA-FL field line–tracing code is used to mimic the full trajectories of the particles outside the LCMS. An alpha-particle loss model based on Monte Carlo drift orbit calculations is first constructed. In Fig. 10a, an example of the alpha-particle exit footprints on the LCMS for such an optimized case are shown, as computed from the ORBIT3D code.[26] In obtaining these footprints, it is assumed that once the guiding center of a drift orbit reaches the LCMS, that particle is considered lost from the plasma. From Fig. 10a, it is found that the alphas escape the plasma almost exclusively through the lower outboard quadrant of the plasma surface, and to a zero-order approximation, the distribution of these exit points is independent of the energy of the escaping particle. As displayed in Fig. 10b, the energy spectrum of the escaping alphas shows a relatively flat distribution in the range of $0.5 < E < 3.5$ MeV; in particular, the number of particles escaping at or near the birth energy of 3.5 MeV is relatively small. For simplicity of analysis, the alpha particles are divided into three

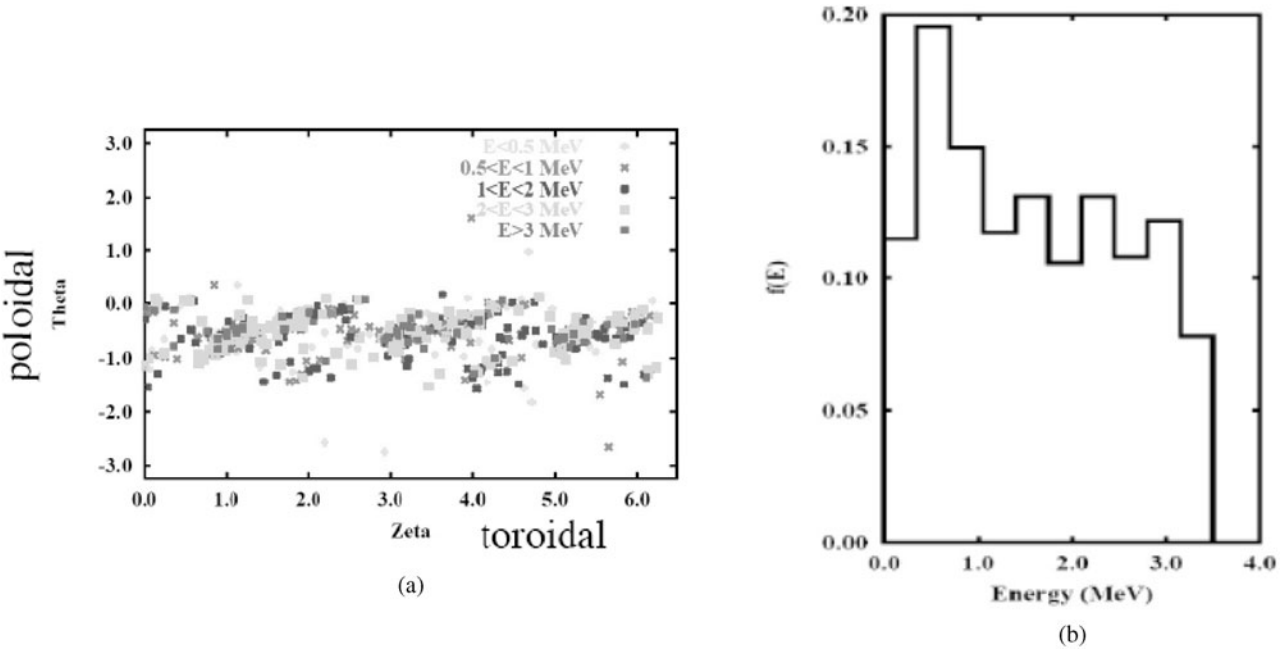

Fig. 10. (a) Alpha-particle exit footprint on LCMS plotted in Boozer (ζ, θ) space. (b) Normalized alpha-particle exit energy spectrum. Both results are from ORBIT3D calculations.

energy groups of equal numbers, centered at 1, 2, and 3 MeV with respective energy ranges of $0.5 < E < 1.5$ MeV, $1.5 < E < 2.5$ MeV, and $2.5 < E < 3.5$ MeV.

Also based on the calculated pitch angle distribution of the escaping alphas,[27] those at the lower end of the energy spectrum and near the birth energy would more likely exit the plasma with toroidal drifts in either directions, while those with energies in between would likely drift in the positive toroidal direction. The approximate alpha loss model requires investigation of two extreme cases: (1) the asymmetric drift case, for the $\langle E \rangle = 1$ MeV group drifting equally in both toroidal directions and the $\langle E \rangle = 2$ and 3 MeV groups drifting entirely in the positive toroidal directions, and (2) the symmetric drift case, for all three energy groups drifting equally in both directions. The results from these two cases should provide a reasonable range of assessments for the alpha-related heat loads.

To complete the model construction, the effects of finite gyro-orbits for the energetic particles must be included. For a magnetic field of 6 T, the alpha gyroradius has a range of 1.7 to 4.5 cm for an energy range of 0.5 to 3.5 MeV, which are comparable to the plate offset distance of ~10 cm from the LCMS. In principle, particle trajectories including drift and gyro motions must be followed to determine their exact strike points on the plates and first wall. However, a full numerical analysis can be computationally intensive. For the purpose of assessment, the field line–tracing technique with no diffusion ($D_\perp = 0$) is used to approximate the alpha-particle flux with bundles of adjacent drift orbits to include the effect of finite gyroradius. For lost particles in the three energy groups, centered at 1, 2, and 3 MeV and with their upper energy bounds of 1.5, 2.5, and 3.5 MeV, their outer gyro-orbits centered at the exit points respectively occupy conformal shells of thickness 3.0, 3.8, and 4.5 cm measured from the plasma LCMS, as shown in Fig. 11. Using this premise, the start points for the field lines representing particles in the three energy groups are uniformly distributed in the three shells of corresponding thickness, confined to the lower OB quadrant of the LCMS.

As noted in Sec. II, in the field line–tracing scheme, it is assumed that each launched field line is associated with a fixed identical power flow. With equal numbers of lost alpha particles in the three energy groups, the number of field lines launched for the 3 (2) MeV group will be three (two) times that for the 1 MeV group. Since for the ARIES-CS reference design point, the thermal and alpha powers incident on the divertor plates are the same (see Sec. III), the total number of launched field lines representing the alpha-particle heat flux is set to equal that used for the thermal heat flux.

The distribution of strike points for the escaping alpha particles on the reference target plates described in Sec. IV is now examined. For the asymmetric drift case, 108 975 field lines are launched from the lower OB quadrant of the plasma surface, with ~17% from a 3.0-cm-thick shell for $\langle E \rangle = 1$ MeV particles in both toroidal directions, ~33% from a 3.8-cm-thick shell for $\langle E \rangle = 2$ MeV particles in the positive toroidal direction, and ~50% from

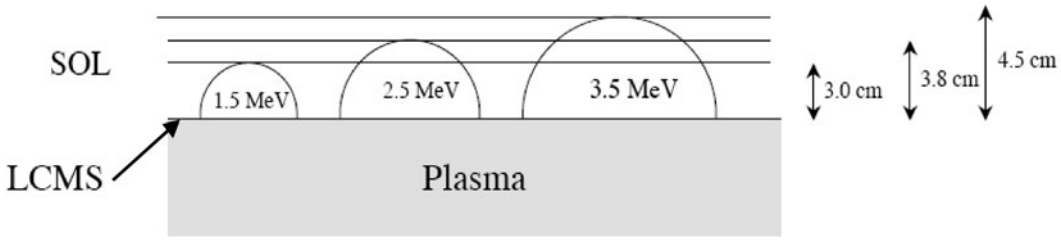

Fig. 11. Three conformal shells with LCMS for launching field lines representing alpha particles with average energies of 1, 2, and 3 MeV.

a 4.5-cm-thick shell for $\langle E \rangle = 3$ MeV alphas also in the positive toroidal direction. Of these, 76.0% strike the plates, 21.2% enter the shadow region, and 2.8% hit the first wall. The strike points on the relevant divertor plates are shown in Fig. 12. As in the case for thermal heat flux, these energetic particles strike all of the target plates but miss entirely one toroidal half of each of the two OB plates. There is a characteristic narrow arc of strike points on each of these OB plates. In Table III, the corresponding alpha-particle heat load distributions on the relevant half-plates for the reference ARIES-CS scenario are presented. Because of the asymmetry of the launch directions of the field lines from the lower half of the plasma, the upper plates intercept 80% of all the alpha heat flux striking the target plates; in particular, the upper IB plate accounts for more than half of all the strike points. In terms of the heat load peaking factor, the LO(+) half-plate registers the highest value of 42.4, with the peak point located in the narrow arc of strike points, as shown in Fig. 13. This translates into the highest peak heat load of 16.8 MW/m^2 among the various half-plates, even though it accounts for only 14.6% of the total alpha-particle heat load incident on the plates.

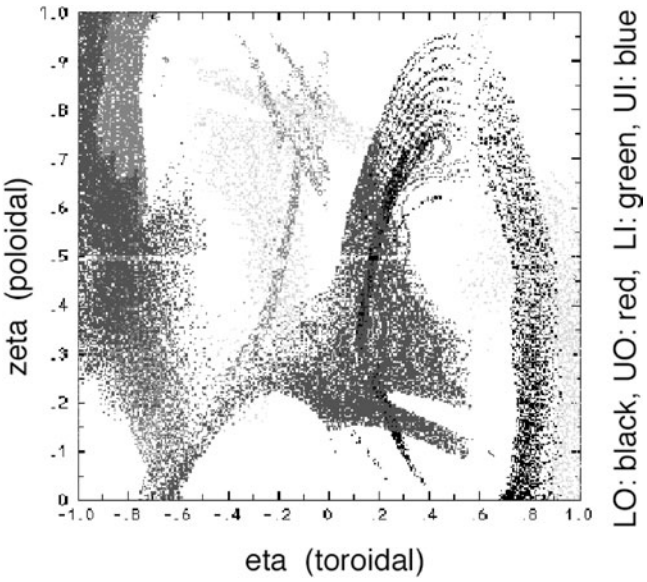

Fig. 12. "Alpha" field line strike points on reference divertor plates plotted in (ξ, ζ) space. (Color online)

The case of symmetric drift has also been investigated for the alpha-particle heat flux, using the same field line launch statistics. The results in terms of the heat load distribution among the half-plates are displayed in Table IV alongside those from the asymmetric drift case for ease of comparison. It is evident that for the asymmetric drift case, most of the alphas strike the upper plates, resulting in a relatively large spread in the peaking factors (9.8 to 42.4) and the peak heat loads (1.7 to 16.8 MW/m^2). On the other hand, when the field lines are launched symmetrically for all energy groups, the alpha particles strike more evenly among the plates, with a narrower spread in peaking factor (11.7 to 20.3) and peak heat load (4.8 to 12.1 MW/m^2) among the half-plates. These comparative results are consistent with basic physics considerations. The correct assessment of the alpha-induced heat load distributions on the plates should lie between the results of these two cases.

VI. COMBINED DIVERTOR HEAT LOAD ASSESSMENTS

Now the results of the heat load calculations for thermal and energetic alpha fluxes can be combined to provide an assessment on the total heat load distribution on the reference divertor configuration. This is accomplished by simply stacking the two sets of calculated strike points into one data set and performing the same type of analysis as described in the previous sections, equivalent to approximately doubling the number of field lines launched.

The case of asymmetric alpha-particle drift is first considered. Out of a total incident power of 47.2 MW, the target plates receive 39.1 MW of combined power (13.0 MW per field period), with 7.5 MW entering the shadow region and 0.7 MW striking the first wall. In real space, the distribution of these powers among the PFCs is displayed in Fig. 14, with strike points on the individual plate surfaces (green dots) and their corresponding

TABLE III

"Alpha" Heat Load Distribution on Reference Divertor Half-Plates

	Half-Plate					
	LO(+)	UO(−)	LI(+)	LI(−)	UI(+)	UI(−)
Load fraction (%)	14.6	27.9	2.9	3.0	25.0	26.5
Incident power (MW)	0.873	1.668	0.173	0.179	1.495	1.585
Area (m^2)	2.20	2.20	2.20	2.02	2.02	2.20
Average load (MW/m^2)	0.397	0.758	0.079	0.089	0.740	0.720
Peaking factor (60×60)	42.36	11.77	30.05	18.82	9.78	14.64
Standard deviation	0.09	0.12	0.22	0.27	0.14	0.12
Peak heat load (MW/m^2)	16.82	8.92	2.37	1.68	7.24	10.54

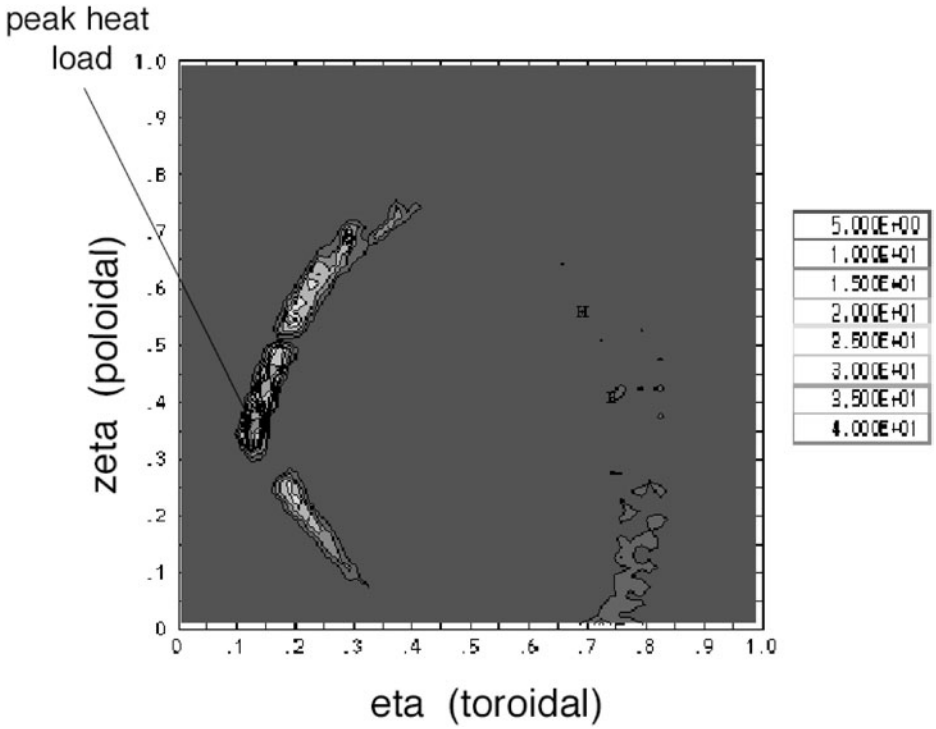

Fig. 13. "Alpha" heat load peaking factor profile on reference LO(+) half-plate in (ξ, ζ) space.

shadow regions (red dots) and on the first wall (blue dots), as viewed from the top of the device. The combined heat load distributions among the relevant half-plates are given in Table IV, labeled as asymmetric, where all the half-plate peak heat loads exceed in value those from the thermal (Table II) and alpha-particle (Table III) heat fluxes alone, as they should. The fact that the combined peak heat loads on the plates are not simply the sums of peak heat loads from the two flux components indicates that the individual peak loads have different locations on those plates. Of the six relevant half-plates, the LO(+) and UO(−) half-plates are found to have the same "alpha" and combined peak heat load locations whereas the rest do not. This leads to the observation that the alpha heat flux may play a dominant role in determining the combined peak heat loads on the target plates. Furthermore, the combined peaking factors for the half-plates are lowered, being influenced by the broader load distribution from the thermal heat flux and/or the larger power incident on the plate. For the asymmetric drift

TABLE IV

Comparison of Combined Heat Load Distributions on Reference Divertor Half-Plates Between Symmetric and Asymmetric "Alpha" Field Line Launch Cases

	Half-Plate					
	LO(+)	UO(−)	LI(+)	LI(−)	UI(+)	UI(−)
Load fraction						
Asymmetric	0.201	0.264	0.050	0.112	0.214	0.159
Symmetric	0.234	0.230	0.103	0.164	0.163	0.105
Incident power (MW)						
Asymmetric	2.617	3.437	0.651	1.458	2.786	2.070
Symmetric	3.047	2.995	1.341	2.135	2.122	1.367
Peaking factor						
Asymmetric	15.48	7.85	17.67	9.49	6.40	13.66
Symmetric	12.32	9.31	14.29	7.07	6.33	14.37
Peak heat load (MW/m^2)						
Asymmetric	18.40	12.26	5.23	6.85	8.83	12.85
Symmetric	17.06	12.67	8.70	7.47	6.65	8.86

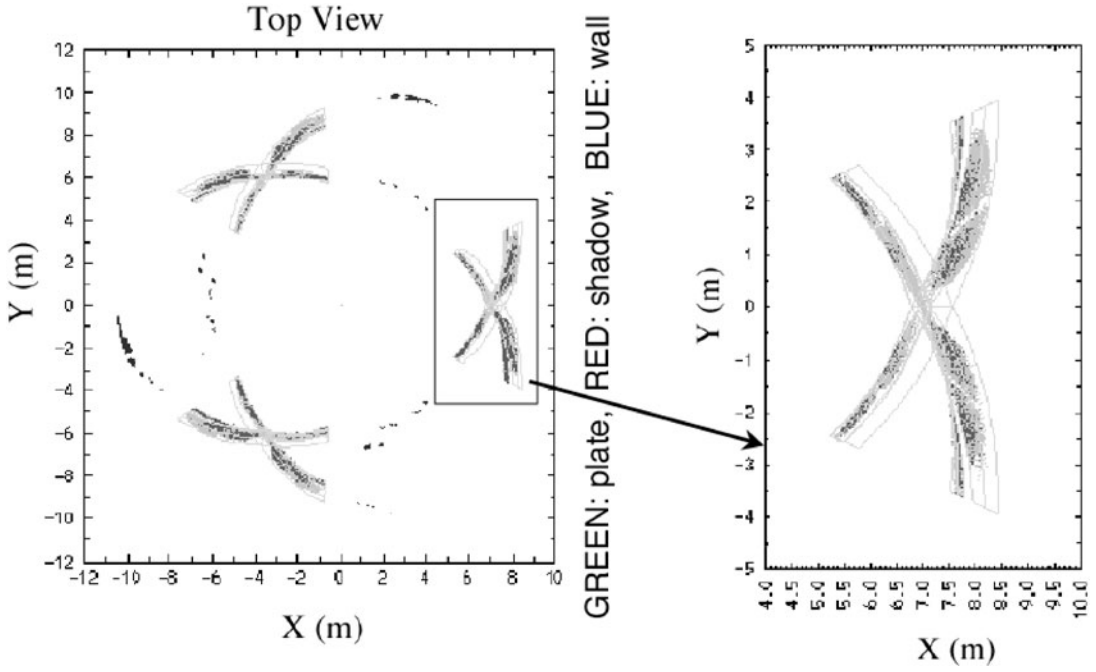

Fig. 14. Top view of combined thermal/alpha field line strike points on plates, in shadow region, and on first wall for reference ARIES-CS case. (Color online)

case, the highest peak heat load is 18.4 MW/m^2 on the LO(+) half-plate, and three out of four plates exceed the 10 MW/m^2 peak heat load limit.

In the other extreme end, where the particles are all assumed to exit in symmetrically drifting orbits, the peak heat loads on the half-plates are somewhat more modest. These are shown in Table IV together with those from the asymmetric drift case. These results indicate that it is likely the combined thermal and energetic alpha heat fluxes from the reference ARIES-CS scenario result in

peak heat loads on the OB plates that far exceed the prescribed limit, with the upper IB plate marginally satisfying the same limit.

VII. SUMMARY AND CONCLUSIONS

In this divertor study for ARIES-CS, a reference target plate geometry has been reached that could potentially perform the task of handling the heat load from thermal fuel and energetic alpha particles. This divertor configuration consists of four plates in each field period that are located one pair each at the top and bottom tips of the crescent-shaped plasma cross section and extend 50 deg in the toroidal direction with a poloidal extent of 20 deg for each plate. An assessment of the total heat load distribution on each plate was accomplished based on power balance for the reference plasma operating conditions. Heat fluxes were included from both the thermal particles and the escaping energetic alpha particles making use of the technique of field line tracing and simplifying assumptions. For the alphas, an approximate model was constructed for the kinetic heat flux based on results of guiding center calculations, whereas a conventional model was used to represent the thermal heat flux. The plate location and surface shape were varied to satisfy the engineering peak heat load limit of $W_{lim} = 10$ MW/m^2. Results to date indicate that, for the chosen plate set, the peak heat load is predicted to be in the range between $\sim$5 and $\sim$18 MW/m^2, with one out of four plates per period satisfying the prescribed limit. Clearly, most of the assessed heat flux levels are too high for He-cooled divertor configurations with power plant–relevant heat extraction. On the other hand, there is room for the plate area to expand, since the present plate configuration with suitable extensions to serve as baffles covers only 10.6% of the plasma surface area, which is below the 15% allowed.

These results point to the need for a full optimization study in the future that will achieve full compliance with the engineering limits. With experience gained in this study, two general ways have been identified to improve on the performance of the present divertor:

1. to reduce the power loss from the main plasma
2. to lower the peaking factor on the target plates.

The most straightforward avenue to achieve the former is to adjust the plasma operating point of ARIES-CS to a higher-density, lower-temperature regime, consistent with physics constraints, in order to further reduce the alpha-particle heat loss from the plasma. At the same time, the assumed values of radiation fractions in the core and in the SOL may be extended toward their limits to further spread the thermal heat flux to the surrounding first wall, thus lowering the power striking the target plates. On the other hand, an optimization of the divertor plate location and spatial extent and the surface topology of the individual plates, a procedure more comprehensive than reported in this paper, should be carried out to further reduce the peaking factors for the plates. The constraints placed on the plate configuration and geometry, such as stellarator symmetry, may be relaxed in this effort of further optimization.

Several improvements to the field line–tracing analysis should be considered. Because the plate has zero thickness in the model, the issue of some field lines striking the side area of the plates in actual devices is not treated, and the edge surface may be contoured to address this problem. If turbulence indeed drives the radial power flux, one would expect some poloidal asymmetry of the thermal flux at the edge. This raises an uncertainty to the assumption that each field line carries the same power. To examine this effect, it may be necessary to impose a nonuniform poloidal distribution of the power associated with the field lines. Furthermore, the sensitivity of the thermal load distribution to the assumed diffusivity should also be investigated.

It should be emphasized that the study described in this paper represents an initial attempt at semiquantitatively evaluating the heat load distribution on divertor plates for a conceptual fusion power plant based on the compact stellarator concept. That energetic particle heat flux is a nonnegligible component of the heat load makes this a rather challenging problem. From this study it is concluded that the alpha-particle heat flux can play a prominent role in determining the peak heat load on the divertor plates. This underscores the need for an improved 3-D physics analysis of the alpha-particle heat flux exiting the plasma and its deposition pattern on the various PFCs, including the effect of their finite gyroorbits. Improvements to the field line–tracing code used in this study to facilitate a large number of case studies employing a sufficient number of field lines should be implemented. Benchmarking of the approximate methods reported here with the implementation of a gyroorbit code to follow the energetic particles in the SOL and future experiments using neutral beams to simulate energetic particle behavior should be pursued. In the longer term, comprehensive physics modeling of the 3-D edge for the compact stellarator, including coupled plasma fluid and neutral transport calculations, and full gyroorbit computations for the escaping alphas should be carried out to validate the results presented in this study.

As a final comment, the divertor configuration described in this paper was determined through a series of optimization steps performed within a number of fixed spatial constraints that were set by physics, engineering, and cost considerations. Examples of the spatial constraints, including the major radius of 7.75 m and the 50 deg toroidal extent placed on the plate geometry, could potentially limit the optimization of the divertor heat load performance. Likewise, the magnetic topology of the reference CS equilibrium, optimized for high beta

and low alpha loss, may also have narrowed the choice of divertor configurations. The lesson drawn is that in future CS reactor studies, the divertor design effort should be carried out concurrently and interactively with the rest of the design effort.

ACKNOWLEDGMENTS

This work was performed under the auspices of the U.S. Department of Energy, Office of Science grant DE-FG02-04ER 54757 (University of California, San Diego), contract W-7405-ENG-48 (Lawrence Livermore National Laboratory), contract DE-AC05-00OR22725 (Oak Ridge National Laboratory), and contract DE-AC02-76-CHO-3073 (Princeton Plasma Physics Laboratory). The authors have benefited from discussions with other members of the ARIES-CS Team, particularly F. Najmabadi, L. El-Guebaly, H. McGuinness, and D. Steiner.

REFERENCES

1. F. NAJMABADI, A. R. RAFFRAY, and ARIES-CS TEAM, "The ARIES-CS Compact Stellarator Fusion Power Plant," *Fusion Sci. Technol.*, **54**, 655 (2008).

2. R. KÖNIG et al., "The Divertor Program in Stellarator," *Plasma Phys. Control. Fusion*, **44**, 2365 (2002).

3. Y. FENG et al., "3D Edge Modeling and Island Divertor Physics," *Contrib. Plasma Phys*., **44**, 57 (2004).

4. A. KOMORI et al, "Local Island Divertor Experiments on CHS," *J. Nucl. Mater*., **241–243**, 967 (1997).

5. T. MORISAKE et al., "Local Island Divertor Experiments on LHD," *J. Nucl. Mater*., **337–339**, 154 (2005).

6. P. GRIGULL et al., "First Island Divertor Experiments on the W7-AS Stellarator," *Plasma Phys. Control. Fusion*, **43**, A175 (2001).

7. H. RENNER et al., "Divertor Concept for the W7-X Stellarator and Mode of Operation," *Plasma Phys. Control. Fusion*, **44**, 1005 (2002).

8. F. GADELMEIER et al., "Stationary and Transient Heat Load in the Island Divertor of W7-AS," *Plasma Phys. Control. Fusion*, **46**, 711 (2004).

9. E. STRUMBERGER, "SOL Studies for W7-X Based on the Island Divert Concept," *Nucl. Fusion*, **36**, 891 (1996).

10. P. C. STANGEBY, *The Plasma Boundary of Magnetic Fusion Devices*, IoP Publishing, Bristol, United Kingdom (2000).

11. Y. FENG, F. SARDEI, J. KISSLINGER, and P. GRIGULL, "A 3D Monte Carlo Code for Plasma Transport in Island Divertors," *J. Nucl. Mater.*, **241–243**, 930 (1997).

12. H. NEILSEN et al., "Design of the National Compact Stellarator Experiment (NCSX)," *Fusion Eng. Design*, **66–68**, 169 (2003).

13. P. K. MIODUSZEWSKI et al., "Power and Particle Handling and Wall Conditioning in NCSX," *Fusion Sci. Technol*., **51**, 238 (2007).

14. A. GROSSMAN, T. KAISER, and P. MIODUSZEWSKI, "Magnetic Structure at the Edge of a Compact Stellarator (NCSX)," *J. Nucl. Mater.*, **337–339**, 400 (2005).

15. R. MAINGI et al., "Magnetic Field Line Tracing Calculations for the Conceptual PFC Design in the National Compact Stellarator Experiment," *Proc. EPS 2006 Conf.*, Paper P5.116 (2006).

16. T. K. MAU et al., "Exploratory Divertor Heat Load Studies for Compact Stellarator Reactors," *Proc. 21st IEEE/NPSS Symp. Fusion Engineering*, Knoxville, Tennessee (2005).

17. L. P. KU et al., "Physics Design for ARIES-CS," *Fusion Sci. Technol.*, **54**, 673 (2008).

18. A. R. RAFFRAY et al., "Engineering Design and Analysis of the ARIES-CS Power Plant," *Fusion Sci. Technol.*, **54**, 725 (2008).

19. L. EL-GUEBALY et al., "Designing ARIES-CS Compact Radial Build and Nuclear System: Neutronics, Shielding, and Activation," *Fusion Sci. Technol.*, **54**, 747 (2008).

20. K. BORRASS, "Disruptive Tokamak Density Limit as Scrape-Off Layer/Divertor Phenomenon," *Nucl. Fusion*, **31**, 1035 (1991).

21. S. P. HIRSHMAN, W. VAN RIJ, and P. MERKEL, "Three-Dimensional Free Boundary Calculations Using a Spectral Green's Function Method," *Comput. Phys. Commun.*, **43**, 143 (1986).

22. E. STRUMBERGER, "Finite-β Magnetic Field Line Tracing for Helias Configurations," *Nucl. Fusion*, **37**, 19 (1997).

23. T. B. KAISER, D. A. MONTECELLO, D. N. HILL, and M. V. UMANSKY, "Heat Load on the NCSX First Wall," *Bull. Am. Phys. Soc.*, **48**, 304 (2003); see also T. B. KAISER and D. N. HILL, "Effect of Divertors in NCSX," *Bull. Am. Phys. Soc*., **49**, 313 (2004).

24. J. F. LYON, L. P. KU, L. EL-GUEBALY, L. BROMBERG, L. M. WAGANER, M. C. ZARNSTORFF, and ARIES-CS TEAM, "Systems Studies and Optimization of the ARIES-CS Power Plant," *Fusion Sci. Technol.*, **54**, 694 (2008).

25. T. IHLI, A. R. RAFFRAY, S. I. ABDEL-KHALIK, S. SHIN, and ARIES-CS TEAM, "Design and Performance of the Helium-Cooled T-Tube Divertor Concept," *Fusion Eng. Des.*, **82**, 249 (2007).

26. R. B. WHITE and M. S. CHANCE, "Hamiltonian Guiding Center Drift Orbit Calculation for Plasmas of Arbitrary Cross Section," *Phys. Fluids*, **27**, 2455 (1984).

27. L. P. KU, Personal Communication (2006).